

## RESEARCH OUTPUTS / RÉSULTATS DE RECHERCHE

### **A two-in-one superhydrophobic and anti-reflective nanodevice in the grey cicada Cicada orni (Hemiptera)**

Dellieu, Louis; Sarrazin, Michaël; Simonis, Priscilla; Deparis, Olivier; Vigneron, Jean Pol

*Published in:*  
Journal of Applied Physics

*DOI:*  
[10.1063/1.4889849](https://doi.org/10.1063/1.4889849)

*Publication date:*  
2014

*Document Version*  
Peer reviewed version

[Link to publication](#)

*Citation for published version (HARVARD):*  
Dellieu, L, Sarrazin, M, Simonis, P, Deparis, O & Vigneron, JP 2014, 'A two-in-one superhydrophobic and anti-reflective nanodevice in the grey cicada Cicada orni (Hemiptera)' Journal of Applied Physics, vol. 116, no. 2, 024701. <https://doi.org/10.1063/1.4889849>

#### **General rights**

Copyright and moral rights for the publications made accessible in the public portal are retained by the authors and/or other copyright owners and it is a condition of accessing publications that users recognise and abide by the legal requirements associated with these rights.

- Users may download and print one copy of any publication from the public portal for the purpose of private study or research.
- You may not further distribute the material or use it for any profit-making activity or commercial gain
- You may freely distribute the URL identifying the publication in the public portal ?

#### **Take down policy**

If you believe that this document breaches copyright please contact us providing details, and we will remove access to the work immediately and investigate your claim.

# A two-in-one superhydrophobic and anti-reflective nanodevice in the grey cicada *Cicada orni* (Hemiptera)

Louis Dellieu,<sup>1, a)</sup> Michaël Sarrazin,<sup>1, b)</sup> Priscilla Simonis,<sup>1</sup> Olivier Deparis,<sup>1</sup> and Jean Pol Vigneron<sup>1, c)</sup>

<sup>1</sup>Research Center in Physics of Matter and Radiation (PMR), Department of Physics, University of Namur (FUNDP), 61 rue de Bruxelles, B-5000 Namur, Belgium

Two separated levels of functionality are identified in the nanostructure which covers the wings of the grey cicada *Cicada orni* (Hemiptera). The upper level is responsible for superhydrophobic character of the wing while the lower level enhances its anti-reflective behavior. Extensive wetting experiments with various chemical species and optical measurements were performed in order to assess the bi-functionality. Scanning electron microscopy imaging was used to identify the nanostructure morphology. Numerical optical simulations and analytical wetting models were used to prove the roles of both levels of the nanostructure. In addition, the complex refractive index of the chitinous material of the wing was determined from measurements.

PACS numbers: 87.19.-j, 42.79.Wc, 68.08.Bc

## I. INTRODUCTION

For a long time, anti-reflective properties have a major importance in the development of optical devices. For instance, anti-reflective coatings are required when designing telescopes, camera lenses, or glass windows. Such coatings allow e.g. avoiding undesirable reflections in optical imaging<sup>1</sup>. Moreover, since anti-reflective coatings are wavelength-dependent, they can be used to reject efficiently unwanted radiation, for instance to enhance ultraviolet light protection in sunglasses<sup>1</sup>. In another context, superhydrophobicity is a key property for numerous industrial applications<sup>2</sup>. Indeed, superhydrophobic surfaces can exhibit self-cleaning properties: since water droplets cannot stick on such a surface, the rolling drops clear the surface from any impurities<sup>3</sup>. As a matter of fact, an optical device that could combine both anti-reflective and superhydrophobic properties is highly interesting<sup>4</sup>.

Anti-reflection is well known in biological organisms: e.g. nanostructures such as nipple arrays act as an adaptative refractive index layer in moth eyes for instance<sup>5,6</sup>. On the other hand, superhydrophobicity is also well-known in many plants<sup>7-14</sup>, for instance in lotus<sup>11,12,15,16</sup>. Hydrophobic properties and antireflecting nanostructures of cicada wings have been studied independently in previous works<sup>17-22</sup>. Although the function as well as the physics of nipple arrays is well documented from the point of view of either antireflection<sup>18</sup> or hydrophobicity<sup>19-22</sup>, the understanding of the role of the geometry in the interplay between optical and wetting properties deserves further investigations. Indeed, the combined aspect of wetting/hydrophobic/anti-reflective properties has not yet been considered as such, strictly speaking. Hereafter, thanks to extensive modeling and

measurements, we show that the grey cicada combines both hydrophobic and anti-reflective properties in an entangled two-level nanostructure. Especially, wetting and hydrophobic properties are studied for a wide range of liquids with various surface tensions. In addition, we determine the complex refractive index of the wing, which is useful and often needed as reference in biophotonics simulations.

## II. MORPHOLOGY AND STRUCTURAL MODEL OF THE WING MEMBRANE

The grey cicada (Fig. 1) is one of the most frequent cicada species in the south of France. The studied specimen was captured at Alés in the Cévennes region. The grey cicada is about 40 mm long and has a 75 mm wing span. In order to investigate the nanostructure of the wing, scanning electron microscopy (SEM) imaging was performed with *Jeol 7500 F* scanning electron microscope.

Both sides of the wing are covered by a hexagonal nipple array (Fig. 2(a)). Each protuberance is a truncated cone, with a hemispherical top (Fig. 2(b)). Protuberances lay on a 2.7  $\mu\text{m}$ -thick slab. This type of protuberance is often encountered in compound eyes or corrugated wings of insects<sup>5,23-25</sup>. According to SEM pictures, the



FIG. 1. (Color online). The grey cicada *Cicada orni* (Hemiptera).

<sup>a)</sup>Electronic mail: louis.dellieu@unamur.be

<sup>b)</sup>Electronic mail: michael.sarrazin@unamur.be

<sup>c)</sup>Our friend and colleague Prof. Jean Pol Vigneron accidentally died on June 24, 2013, during the early writing of this article.

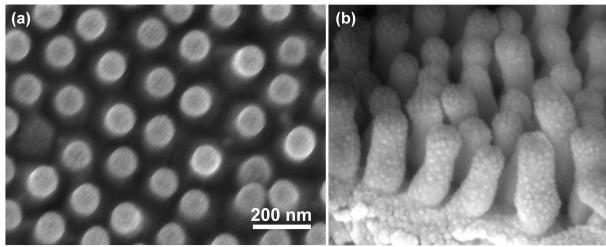


FIG. 2. Scanning electron microscopy images of the cicada wing (same scale for both figures). a: Typical hexagonal nipple array is clearly observed. b: Protuberances consist of conic-like tips with a hemispherical top.

typical dimensions and geometry of the different parts of the structure can be estimated on average (see Fig. 3(a)). The truncated cone has a circular base of radius  $R \approx 85$  nm, and a height  $h \approx 160$  nm. The top hemisphere has a radius  $r \approx 40$  nm. The total height (cone + hemisphere) is therefore  $H \approx 200$  nm. The average hexagonal lattice parameter is  $a_0 \approx 173$  nm. We fairly assume that the disorder in the biological structure, i.e. weak deviations with respect to perfect lattice, does not significantly affect the main conclusions of the present study<sup>26</sup>.

### III. OPTICAL PROPERTIES

In the following, we highlight the anti-reflective properties of the cicada wing through scattering and transmission measurements. Based on models of the wing structure, simulations were performed in order to study the role of the morphology on the optical properties.

#### A. Experimental results

The diffusive and polarizing characters of the wing were investigated at incidence angles  $i$  of  $0^\circ$ ,  $15^\circ$  and  $30^\circ$  using scatterometry in transmittance mode (*ELDIM EZ-contrast* scatterometer). This scatterometer uses Fourier lenses to record the bidirectional transmittance or reflectance distribution function (BTDF or BRDF) of the sample (Fig. 4(a)) at visible wavelengths. In order to detect possible polarization of the emerging light, a polarizer was placed as analyzer as shown in Fig. 4(a). In a first step (calibration), at each incidence angle, the BTDF of the incident beam alone (without wing and polariser) was measured, showing purely specular transmittance as expected (Fig. 4(b)). In a second step, the wing was inserted and the polarizer was positioned perpendicular ( $\alpha = 90^\circ$ ) to the wing longitudinal axis and then parallel to it ( $\alpha = 0^\circ$ ). BTDFs of the wing for both analyzed polarizations were recorded. At each incidence angle  $i$ , both BTDF maps were compared to the BTDF map of the incident beam alone. As polarization effects

should be observed preferably at large incidence angles, the results in Fig. 4(c) and 4(d) are presented for the incidence angle  $i$  of 30 degrees (and a wavelength  $\lambda \cong 510$  nm in the middle of visible range). Accordingly, neither diffusive effects nor polarizing effects of the wing could be detected (Fig. 4(c) and 4(d)). Results (not shown) were identical for the other wavelengths in the visible spectrum (according to the characteristics of our scatterometer). Since the wing exhibited a very low diffusive character and in order to optimize the signal to noise ratio, transmission properties are mainly emphasized hereafter by contrast with reflection properties.

Measurement of the wing optical properties spectrum were performed at normal incidence using a double beam spectrophotometer (*Perkin Elmer Lambda 750 S UV/VIS/NIR*) and an integrating sphere. In Fig. 5(a), reflection spectrum is shown. Since reflection is very weak, measurement was made with the wing on a black substrate (Certified Reflectance Standard SRS-02-020 *Labsphere* with a reflectance factor of 2% between 250 and 2500 nm). The measured reflection  $R_m$  had to be corrected since  $R_m$  was fairly approximated by  $R_m \approx R_w + R_{bg} \cdot T_w^2$  (see insert in Fig. 5(a)) where  $R_w$  was the expected wing reflection,  $R_{bg}$  was the black substrate reflection (which was measured independently, not shown), and  $T_w$  was the free-standing wing transmission which is measured independently (see hereafter). In Fig. 5(a), the blue dashed curve is  $R_m$  whereas the black solid curve is  $R_w$  which is deduced from the above expression. This correction confirms that reflection values are weak in accordance with previous results<sup>18</sup>, and must be derived carefully. In addition, it is well-known that spectroscopic measurements are impacted by instrumental noise for low transmittance or reflectance levels. As a consequence, it is more relevant to compare high-level transmittance measurements with numerical mod-

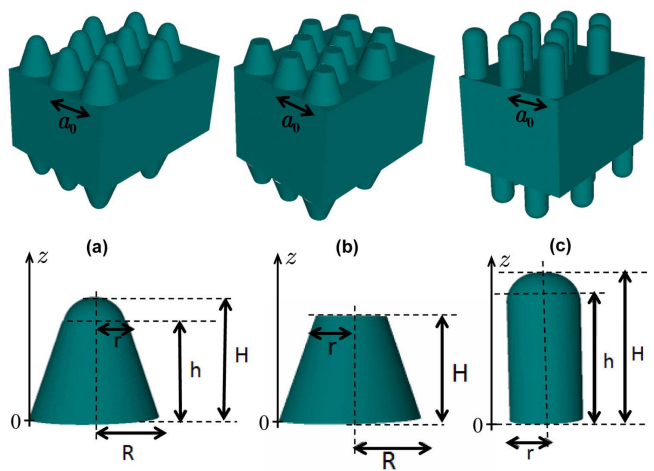


FIG. 3. (Color online). Various geometrical models studied. a: Model of the wing structure, b: Model used to study the influence of top hemisphere on transmission, c: Model used to study the influence of truncated cone on transmission.

els, rather than low-level reflectance measurements.

Let us now consider transmission measurements. They were carried out on free-standing wings i.e without substrate. The black curve in Fig. 5(b) indicates an almost perfect transmission in the visible range although it appears to be weaker on the blue side than on the red side of the spectrum. This means that almost 100% of the light passes through the free-standing wing without being absorbed or reflected. The transmission exhibits a large drop below 350 nm, due to a strong intrinsic absorption in the ultra-violet range. Note that in Fig. 5(a) we found that reflection does not fade away at these wavelengths. Using the absorption coefficient calculated from reflection and transmission at each wavelength, the spectrum of the imaginary part of the complex refractive index was deduced from the Beer-Lambert law<sup>27</sup> as shown in Fig. 5(c).

In order to reveal the effect of the nipple array on the optical properties, the wing was covered with a calibrated refractive-index oil. Indeed, provided that the oil refractive index matches the refractive index of the protuberances, the oil filling the air cavities and the material can be regarded as a single planar layer. Here, a decrease of transmission was noted using a calibrated commercial oil with a real part of refractive index equal to 1.56 (see blue dashed curve on Fig. 5(c)). This oil is certified by the manufacturer *Cargille Labs* (also verified by us) with a negligible dispersion on the visible range and a weak dispersion in the ultraviolet domain. Such a refractive-index value is consistent with that of chitin<sup>28</sup>. As a result, in the following, we will assume that the cicada wing is made of a chitin-like compound with an average refractive index of 1.56. On Fig. 5(b), the blue dashed curve (transmission spectrum of wing immersed in index matching oil) shows a transmission drop of 6% in the visible range and spectral changes in the UV range. One can then conclude that the nipple array increases the transmission by 6%, improving the transparency of the wing. These results are in agreement with those obtained by other authors<sup>18</sup>. Since UV absorption of the chitin material was determined, the absorption coefficient of the wing (extrapolated from experimental measurement) (Fig. 5(c)) will be used in the following numerical simulations.

## B. Theoretical analysis

On the basis of morphological data, we described the wing as a homogeneous slab with, on both side, a hexagonal array of truncated cones with top hemisphere (Fig. 3(a)). For the sake of simplicity, we assumed that the wing was made of chitin only. The real part of the refractive index was taken equal to 1.56 and was assumed to be constant all over the simulation spectral range whereas the absorption coefficient was taken wavelength-dependent according to data shown in Fig. 5(c). Simulations of the optical properties were carried out from the

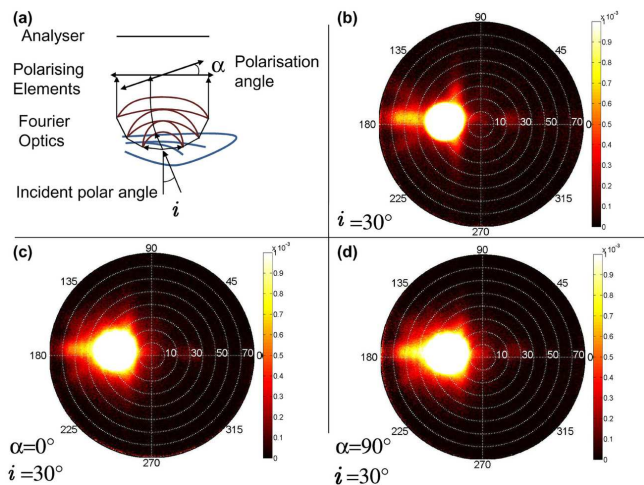


FIG. 4. (Color online). Bidirectional Transmittance Distribution Functions (BTDF) (in  $\text{watt/m}^2/\text{sr}/\text{nm}$ ). Results are shown for polar angles ranging from  $0^\circ$  to  $80^\circ$  and azimuthal angles in ranging from  $0^\circ$  to  $360^\circ$ . The wavelength is  $\lambda = 509.48$  nm. a: Principle of the scatterometer. b: BTDF of the incident beam at an angle of incidence  $i = 30^\circ$ . c,d: BTDF of the cicada wing at  $i = 30^\circ$  and for two orthogonal analyzing polarizer orientations,  $0^\circ$  (panel (c)) and  $90^\circ$  (panel (d)).

near UV to the near infrared (200 to 800 nm) by using a transfer matrix code<sup>26</sup>.

Since the nipple array has subwavelength dimensions, the corrugated layer can be considered as a continuous effective material with a graded-index along its thickness. More specifically, the effective dielectric constant can then be defined by<sup>5</sup>:

$$\varepsilon(z) = \varepsilon_{air} + (\varepsilon_{chitin} - \varepsilon_{air})f(z), \quad (1)$$

where  $\varepsilon_{air}$  is the dielectric constant of air ( $\varepsilon_{air} = 1$ ),  $\varepsilon_{chitin}$  is the dielectric constant of chitin and  $f(z)$  is filling factor given by:

$$f(z) = \frac{\pi r^2(z)}{S}, \quad (2)$$

with  $S = \frac{a_0^2 \sqrt{3}}{2}$  and  $r(z)$  the radius of the circular section of a nipple at coordinate  $z$ . While light propagation in corrugated layers is computed thanks to the transfer matrix code, light propagation in the homogeneous thick slab is calculated using an analytical expression based on Fresnel equations in which phases are set to zero in order to mimic optical incoherence. Indeed, structural imperfections in the slab, which is a thick biological layer, tend to break constructive light wave interferences. Finally, although we choose to focus on transmission for the reasons we exposed previously, simulations of reflection are also performed to corroborate our results.

Simulation results for transmission are shown in Fig. 6(a). The black curve corresponds to the measured trans-

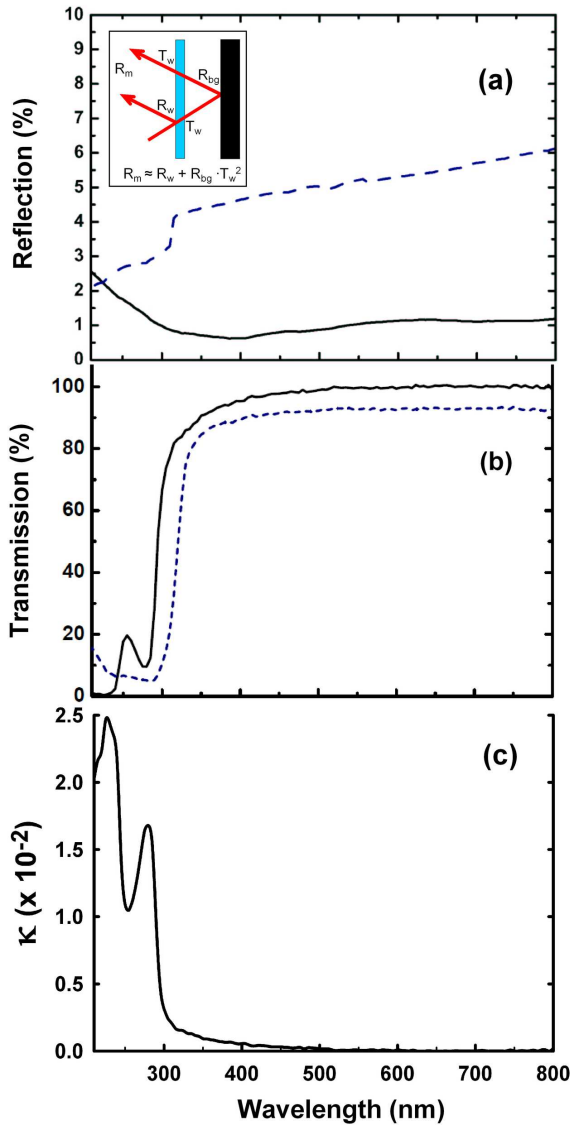


FIG. 5. (Color online). a: Measured wing reflection spectrum at normal incidence (blue dashed curve) and corrected measurement (black solid curve). Insert: Correction procedure. b: Measured wing transmission spectrum. Measurements on the actual free-standing wing (black curve) and the wing immersed in index matching oil (blue dashed curve). c: Imaginary part of the optical index of the cicada wing obtained from reflection/transmission measurements.

mission whereas the red curve corresponds to the simulated transmission: The two curves match very well. This result is valid whatever the polarization state is. In order to discriminate the role of the truncated cone and the role of the top hemisphere, two alternative wing models were considered. We first considered a truncated cone without the hemisphere on top (see Fig. 3(b)). Fig. 6(b) shows the simulated spectrum (red curve) and the measured spectrum (black curve). Both transmission spectra match quite well, showing that the hemisphere does not actually contribute to the transparency of the wing. In

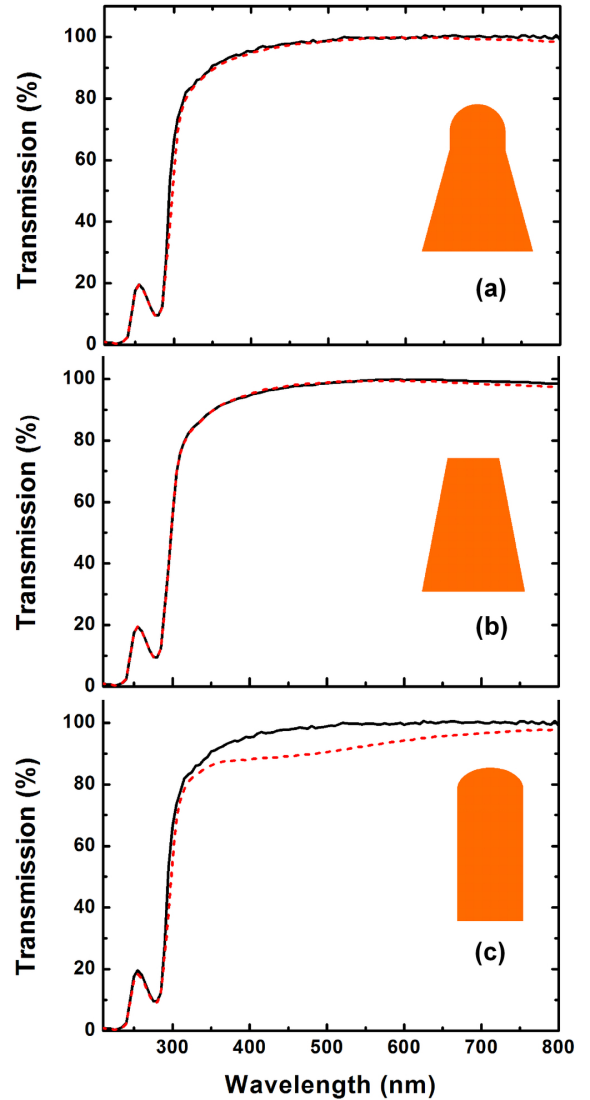


FIG. 6. (Color online). a: Measurement (black solid curve) and theoretical simulation (red dashed curve) on the actual wing model. b: Measurement (black solid curve) vs. theoretical simulation on the wing model without hemispheres on top (red dashed curve). c: Measurement (black solid curve) vs. theoretical simulation on the wing model with cylinders instead of truncated cones (red dashed curve).

a second simulation, we considered a cylinder (instead of a cone) (see Fig. 3 (c)) with a hemisphere on top. The result is shown in Fig. 6(c). The simulated transmission (red curve) is significantly lower than the measured one (black curve). Together with the previous simulation, this result shows that the truncated cone is required to get transparency in the visible range. This can be easily understood since the truncated cone avoids a sudden change in the refractive index when light impinges on the slab. Indeed, considering Eq. (1), the truncated cone creates a gradient of refractive index which acts as an optical impedance adaptation layer.

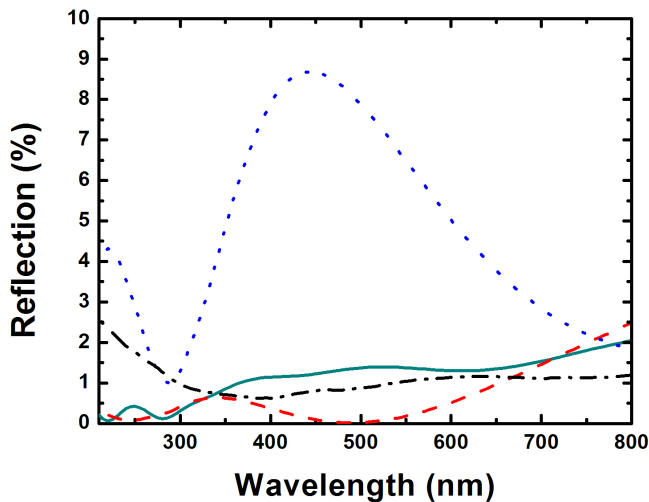


FIG. 7. (Color online). Theoretical simulation (red dashed curve) of the reflection on the full wing model (Fig. 3 (a)). This curve can be compared with the simulated reflections for the wing model without hemispheres on top (cyan solid curve) or with cylinders instead of truncated cones (blue short-dashed curve). The black dash-dotted curve is the measured reflection.

Let us now consider the simulated reflection. Our results are summarized in Fig. 7. The measured (black dash-dotted curve) and simulated (red dashed curve) reflections exhibit comparable values about 1%. Nevertheless, we note that spectra of both reflections do not perfectly match. As explained previously, this can be explained by the lack of accuracy when measuring weak reflections. We also present the simulated reflection for the wing model without hemispheres (cyan solid curve). As for the transmission (Fig. 6(b)), there is negligible difference (less than 2%) with the full wing model (Fig. 3(a)). Now, by contrast, if we consider the model with cylinders instead of truncated cones, we see that the reflection increases by a factor 10. This corroborates qualitatively our results obtained with the transmission (Fig. 6(c)). In addition, we note the strong oscillations of the simulated reflection, since the array of cylinders acts as a thin effective homogeneous slab where interferences can occur.

#### IV. WETTING PROPERTIES

In this section, contact angle measurements are reported and wettability regimes are investigated. Analytical models are used to describe the superhydrophobicity of the wing.

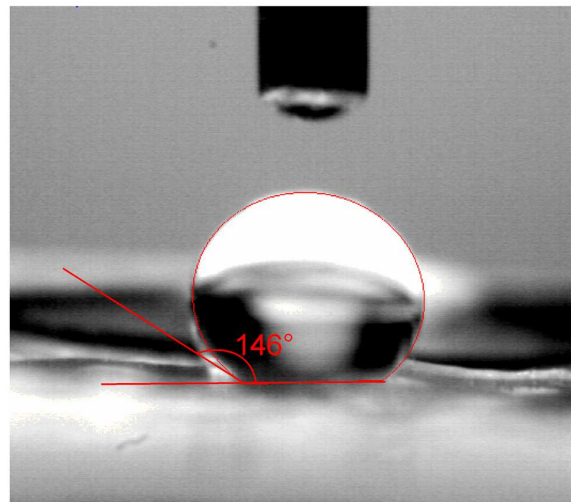


FIG. 8. (Color online). Wetting measurement on wing of *Cicada orni*, the contact angle is  $146^\circ$ .

#### A. Experimental results

A surface can be classified as superhydrophobic if the contact angle of a water droplet on the surface is higher than  $150^\circ$ . If the contact angle lies between  $90^\circ$  and  $150^\circ$ , the surface is only hydrophobic and it is hydrophilic if the contact angle lies between  $0^\circ$  and  $90^\circ$ . In the present case, the contact angle of a water droplet on the wing surface is measured to be  $146^\circ$  (Fig. 8). As a consequence, the wing of *Cicada orni* is almost superhydrophobic. According to previous works related to the link between nanostructure and superhydrophobicity<sup>20,23,29-31</sup>, we can fairly assess that the nipple array covering the wing surface is responsible for its hydrophobic properties (see Fig. 9). Indeed, without the nanostructure, the water droplet would probably spread on the surface since the contact angle of water on a flat chitin surface is about  $105^\circ$ <sup>32</sup>.

For a better understanding of the wing hydrophobicity, it is relevant to measure the wetting properties for various liquids with different surface tensions. For this purpose, we used ethanol-water solutions with different mass percentages of ethanol (from 0% to 100%), but also a 6.0 M sodium chloride aqueous solution and mercury.

The effective contact angle  $\theta_{eff}$  for each liquid on the wing (the nanostructured surface) was measured, and  $\cos\theta_{eff}$  was plotted against  $\cos\theta_0$ , where  $\theta$  is the contact angle on a flat chitin surface (Fig. 10 ; black dots correspond to measured values). Since the liquid-gas surface tension  $\gamma_{LG}$  of the used liquids are known<sup>33-35</sup>, and since the solid-gas surface tension  $\gamma_{SG}$  of chitinous material can be calculated (see further), it is possible to calculate the contact angle  $\theta_0$  for a given liquid on a flat chitinous surface, using the Young equation<sup>3</sup>:

$$\gamma_{SG} = \gamma_{SL} + \gamma_{LG} \cos\theta_0. \quad (3)$$

Knowing that solid/liquid surface tension  $\gamma_{SL}$  can be ap-

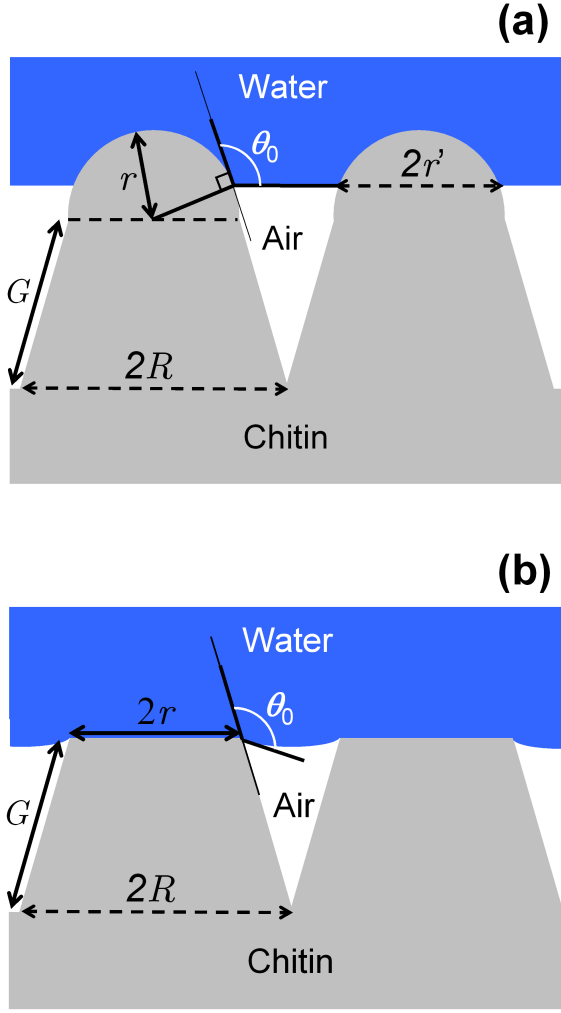


FIG. 9. (Color online). Wetting models under consideration. a: Wetting model from the full cicada's wing description. b: Wetting model without hemispheric top. The angle  $\theta_0$  corresponds to the Young's contact angle for a flat chitin surface.

proximated by<sup>3</sup>:

$$\gamma_{SL} \approx \gamma_{SG} + \gamma_{LG} - 2\sqrt{\gamma_{SG}\gamma_{LG}}, \quad (4)$$

we then get

$$\cos \theta_0 = 2\sqrt{\frac{\gamma_{SG}}{\gamma_{LG}}} - 1 \quad (5)$$

from Eqs (3) and (4). Since  $\gamma_{LG}$  of water is known, as well as the contact angle of a water droplet on flat chitinous surface ( $\theta_0 = 105^\circ$ )<sup>32</sup>, we deduce from (3)  $\gamma_{SG} \approx 9.9 \times 10^{-3} \text{ N}\cdot\text{m}^{-1}$ . In Fig. 10, gold and red lines denote the linear asymptotic trends in data when  $\cos \theta_{eff} < 0$ , i.e. when the wing is not wet. By contrast, the blue line denotes the behavior of the wet wing ( $\cos \theta_{eff} > 0$ ), i.e. the hydrophilic regime. The horizontal green line corresponds to the process of hemiwicking<sup>36,37</sup>. According to these results, we observe a transition from a superhydrophobic regime to a hydrophilic regime.

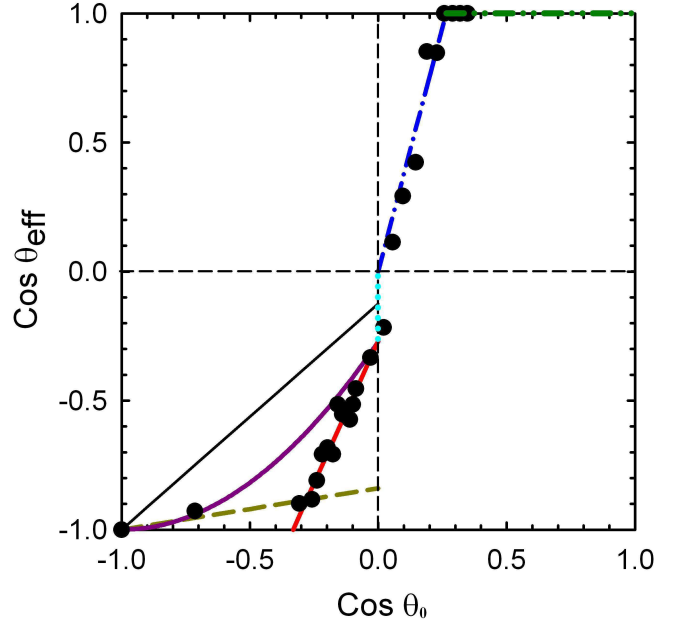


FIG. 10. (Color online). Effective contact angle  $\theta_{eff}$  (nanostructured surface) as a function of the contact angle  $\theta_0$  on a flat surface. The black dots are the experimental results. The blue (dash-dotted) straight line is plotted from Eq. (9), the purple (solid) curve is from Eq. (7). Gold (dashed) and red (solid) straight lines show trends by contrast to the ideal model. Light blue (dotted) vertical straight line corresponds to the hydrophobic/wetting transition. The green (dash-dotted) straight line corresponds to the process of hemiwicking. Black solid line is plotted from Eq. (8).

## B. Theoretical analysis

Models of wetting processes are used hereafter in order to predict the contact angle of a water droplet on the wing. Specifically, they are used to describe the superhydrophobic, hydrophobic or hydrophilic behavior of the wing. Two theoretical models are considered: the Cassie-Baxter model for the hydrophobicity regime and Wenzel model for the hydrophilic regime.

The Cassie-Baxter (CB) model<sup>38</sup> allows to describe the wetting process on superhydrophobic and hydrophobic surfaces according to their roughness (i.e. nipple array). For a surface made of two different materials with different coverage areas, the contact angle  $\theta_{CB}$  of the heterogeneous surface is given by:

$$\cos \theta_{CB} = f_1 \cos \theta_1 + f_2 \cos \theta_2. \quad (6)$$

where  $f_1$  and  $f_2$  are the fractional areas of each material ( $f_1 + f_2 \geq 1$ ), and  $\theta_1$  and  $\theta_2$  are the contact angles, respectively.

Using the nipple geometry previously described, we consider the wetting model shown on Fig. 9(a). The contact angle in the present case can be written as<sup>39</sup>:

$$\cos \theta_{CB} = n\pi r^2(1 + \cos \theta_0)^2 - 1, \quad (7)$$

where  $n$  is the number of hemispheres per unit area for a hexagonal array,  $r$  is the radius of the hemisphere, and  $\theta_0$  is the contact angle of a droplet deposited on flat chitin. This well-known equation, can be simply derived from Eq. (6) by assuming that  $\theta_1 = \theta$  and  $\theta_2 = 180^\circ$ . Indeed,  $\theta_2$  is the contact angle between a droplet and air, which is assumed to be  $180^\circ$ . Fractional areas can be easily derived from trivial geometrical considerations. On Fig. 10, Eq. (7) is plotted as the purple curve with  $\theta_{CB} = \theta_{eff}$ , using geometrical parameters mentioned in section II and measured from SEM pictures. Gold and red lines show wetting trends experimentally observed by contrast to the theoretical model<sup>40</sup>. Though the theoretical curve and the experimental data do not perfectly match, the trends are the same. Differences are likely due to the fact that the water/air interface (see Fig. 9(a)) is not truly a planar one, modifying then the conditions for which the Gibbs energy is minimized<sup>3</sup>. Nevertheless, more accurate modeling is a complex task far beyond the scope of the present work<sup>41</sup>.

We note that, using Eq. (7), we find a theoretical contact angle of  $151^\circ$  for water by contrast with the measured value of  $146^\circ$ , i.e there is less than 4% difference between theory and experiment.

In order to clearly demonstrate the essential role of the hemispherical top, we investigated the wetting properties of the conical base structure without the top hemisphere (Fig. 9(b)). In this case, the Cassie-Baxter contact angle is simply given by:

$$\cos \theta_{CB} = f \cos \theta_0 + (f - 1), \quad (8)$$

with  $f = \pi r^2/S$  and  $S = a_0^2\sqrt{3}/2$ . The linear dependence, which is plotted in Fig. 10 as a black solid line, leads to much less satisfactory agreement with data, as compared with the quadratic dependence (purple curve) pertaining to the hemispherical top, i.e. Eq. (7). Indeed, for water ( $\theta_0 = 105^\circ$ ), a theoretical contact angle of  $\theta_{CB} = 111^\circ$  is predicted by Eq. (8), whereas a value of  $151^\circ$  was determined previously by Eq. (7). Therefore, only the model including the hemispherical top is able to account for the superhydrophobicity of the wing.

The hydrophilic behavior of a corrugated surface, on the other hand, can be described thanks to the Wenzel (W) model<sup>42</sup>. In this case, the contact angle is given by:

$$\cos \theta_W = r_o \cos \theta_0, \quad (9)$$

where  $r_o$  is the roughness factor which is in our case given by:

$$r_o = \frac{2\pi r^2 + \pi G(R + r) + a_0^2\sqrt{3}/2 - \pi R^2}{S}, \quad (10)$$

with  $S = a_0^2\sqrt{3}/2$ ,  $r$  the radius of the hemisphere,  $R$  the radius of the base of the cone,  $G$  the length of the cone ( $\approx 166$  nm) and  $a_0$  the spatial period. Equation (8) is a linear relation between the effective contact angle and the contact angle on a flat surface made of the same material. On Fig. 10, Eq. (9) is plotted as blue curve with  $\theta_W = \theta_{eff}$ , using geometrical parameters mentioned in section II and measured from SEM pictures. Here, the model matches very well with the experimental data.

We emphasize the fact that the wetting models underline the role of the top hemisphere in the wetting phenomena, and especially in the hydrophobic behavior of the cicada wings. In the wetting regime, the whole structure geometry must be considered to explain the wetting.

## V. SUMMARY AND CONCLUSION

While it is known that cicada wings possess both hydrophobic<sup>17-19</sup> and anti-reflective properties<sup>5,6</sup>, in the present work we underlined the two-in-one character of the geometrical features leading both to the optical and wetting properties of the cicada. From scanning electron microscopy, it was shown that the cicada wing consisted of a thick chitinous layer whose each side was covered by a nanostructured device in the form of an hexagonal nipple array. Each nipple was modeled by a truncated cone topped by an hemisphere. We performed an original wetting experiment with various chemical species as well as comprehensive optical measurements providing the complex refractive index of the chitinous wing. From optical simulations and using an analytical wetting model, we demonstrated the character of the two functional levels of the nipple array. We concluded that the hemisphere on the top of the nipple was useful for the superhydrophobic character of the cicada wing. This half-sphere played no optical role. By contrast, the truncated cone played no significant role in the hydrophobic behavior while it was found to be fundamental for ensuring transparency of the cicada wing (anti-reflection). Therefore, the nipple array nanostructure in the grey cicada can be considered as a two-in-one device: a hemisphere top which allows a strong water repellency and a truncated cone which ensures anti-reflective properties.

## ACKNOWLEDGMENTS

The authors thank Corry Charlier, Jean-François Colomer, Quentin Spillier and Michaël Lobet for their technical support and advice. L.D. is supported by the Belgian Fund for Industrial and Agricultural Research (FRIA). M.S. is supported by the Cleanoptic project (development of super-hydrophobic anti-reflective coatings for solar glass panels/convention No.1117317) of the Greenomat program of the Wallonia Region (Belgium).

<sup>1</sup>E. Hechts, *Optics* (Addison-Wesley, 4th edition, 2001).



- <sup>2</sup>L. Yan, K. Wang, J. Wu, L. Ye, *Colloids and Surfaces : Physicochem. Eng. Aspects* **296**, 123 (2007).
- <sup>3</sup>H.-J. Butt, K. Graf, M. Kappl, *Physics and Chemistry of Interfaces* (Wiley-VCH, 2005).
- <sup>4</sup>X. Li, J. He, W. Liu, *Materials Research Bulletin* **48**, 2522(2013).
- <sup>5</sup>D.G. Stavenga, S. Foletti, G. Palasantzas, K. Arikawa, *Proc. R. Soc. B* **273**, 661 (2006).
- <sup>6</sup>C.G. Bernhard, *Endeavour* **26**, 79 (1967).
- <sup>7</sup>L. Feng, Y.A. Zhang, J.M. Xi, Y. Zhu, N. Wang, F. Xia, L. Jiang, *Langmuir* **24**, 4114 (2008).
- <sup>8</sup>L. Feng, Y.A. Zhang, M.Z. Li, J.M. Zheng, W.Z. Shen, L. Jiang, *Langmuir* **26**, 14885 (2010).
- <sup>9</sup>B. Bhushan, E.K. Her, *Langmuir* **26**, 8207 (2010).
- <sup>10</sup>K. Koch, W. Barthlott, *Phil. Trans. R. Soc. A* **367**, 1487 (2009).
- <sup>11</sup>W. Barthlott, C. Neinhuis, *Planta* **202**, 1 (1997).
- <sup>12</sup>W. Barthlott, C. Neinhuis, *Ann. Bot.* **79**, 667 (1997).
- <sup>13</sup>P. Ball, *Nature* **400**, 507 (1999).
- <sup>14</sup>L. Feng, S.H. Li, Y.S. Li, H.J. Li, L.J. Zhang, J. Zhai, Y.L. Song, B.Q. Liu, L. Jiang, D.B. Zhu, *Adv. Mater.* **14**, 1857 (2002).
- <sup>15</sup>A. Solga, Z. Cerman, B. F. Striffler, M. Spaeth, and W. Barthlott, *Bioinspir. Biomim.* **2**, S126 (2007).
- <sup>16</sup>N.M. Pugno, *The Nanomechanics in Italy* (Research Signpost, 2007).
- <sup>17</sup>G. Xie, G. Zhang, F. Lin, J. Zhang, Z. Liu, S. Mu, *Nanotechnology* **19**, 095605 (2008).
- <sup>18</sup>M. Sun, A. Liang, Y. Zheng, G.S. Watson, J.A. Watson, *Bioinsp. Biomim.* **6**, 026003 (2011).
- <sup>19</sup>M. Sun, G.S. Watson, Y. Zheng, J.A. Watson, A. Liang, *J. Exp. Biol.* **212**, 3148 (2009).
- <sup>20</sup>G.S. Watson, S. Myhra, B.W. Cribb, J.A. Watson, *Biophys. J.* **94**, 3352 (2008).
- <sup>21</sup>M. Sun, A. Liang, G.S. Watson, J.A. Watson, Y. Zheng, J. Ju, L. Jiang, *PLoS ONE* **7** e35056 (2012).
- <sup>22</sup>K.M. Wisdom, J.A. Watson, X. Qu, F. Liu, G.S. Watson, C.-H. Chen, *PNAS* **110** 7992 (2013).
- <sup>23</sup>D. Byun, J. Hong, Saputra, J.H. Ko, Y.J. Lee, H.C. Park, B. Byun, J.R. Lukes, *J. Bionic Eng.* **6**, 63 (2009).
- <sup>24</sup>O. Deparis, N. Khuzayim, A. Parker, J.P. Vigneron, *Phys. Rev. E* **79**, 041910 (2009).
- <sup>25</sup>A. Yoshida, *Forma* **17**, 75 (2002).
- <sup>26</sup>J.P. Vigneron, V. Lousse, *Proc SPIE* **6128**, 61281G (2006).
- <sup>27</sup>A. Beer, *Ann. Phys. (Berlin)* **162**, 78 (1852).
- <sup>28</sup>A. R. Parker, R. C. McPhedran, D. R. McKenzie, L. C. Botten, N. A. Nicorovici, *Nature* **409**, 36 (2001).
- <sup>29</sup>S.N. Gorb, A. Kesel, J. Berger, *Arthropod Struct. Dev.* **29**, 129 (2000).
- <sup>30</sup>T. Wagner, C. Neinhuis, W. Barthlott, *Acta Zool-Stockholm* **77**, 213(1996).
- <sup>31</sup>Y. Zheng, X. Gao, L. Jiang, *Soft Matter* **3**, 178 (2007).
- <sup>32</sup>M.W. Holdgate, *J. Exp. Biol.* **32**, 591 (1955).
- <sup>33</sup>G. Vazquez, E. Alvarez, J. Navaza, *J. Chem. Eng. Data* **40**, 611 (1995).
- <sup>34</sup>M. Wigglesworth, T. Wood, *Management of Chemical and Biological Samples for Screening Applications* (Wiley-VCH, 2012).
- <sup>35</sup>A.W. Adamson, A.P. Gast, *Physical Chemistry of Surfaces* (John Wiley and Sons Inc., 1997).
- <sup>36</sup>D. Quéré, *Physica A* **313**, 32 (2002).
- <sup>37</sup>C.W. Extrand, S.I. Moon, P. Hall, D. Schmidt, *Langmuir* **23**, 8882 (2007).
- <sup>38</sup>A.B.D. Cassie, *Discuss. Faraday Soc.* **3**, 11 (1948).
- <sup>39</sup>J. Bico, C. Marzolin, D. Quéré, *Europhys. Lett.* **47**, 220 (1999).
- <sup>40</sup>T. Onda, S. Shibuichi, N. Satoh, K. Tsujii, *Langmuir* **12**, 2125 (1996).
- <sup>41</sup>T. Koishi, K. Yasuoka, S. Fujikawa, T. Ebisuzaki, X.C. Zeng, *PNAS* **106**, 8435 (2009).
- <sup>42</sup>R.N. Wenzel, *Ind. Eng. Chem.* **28**, 988 (1936).